

Heterologous Assembly of Pleomorphic Bacterial Microcompartment Shell Architectures Spanning the Nano- to Microscale

Bryan H. Ferlez, Henning Kirst, Basil J. Greber, Eva Nogales, Markus Sutter,*
and Cheryl A. Kerfeld*

Many bacteria use protein-based organelles known as bacterial microcompartments (BMCs) to organize and sequester sequential enzymatic reactions. Regardless of their specialized metabolic function, all BMCs are delimited by a shell made of multiple structurally redundant, yet functionally diverse, hexameric (BMC-H), pseudohexameric/trimeric (BMC-T), or pentameric (BMC-P) shell protein paralogs. When expressed without their native cargo, shell proteins have been shown to self-assemble into 2D sheets, open-ended nanotubes, and closed shells of ≈ 40 nm diameter that are being developed as scaffolds and nanocontainers for applications in biotechnology. Here, by leveraging a strategy for affinity-based purification, it is demonstrated that a wide range of empty synthetic shells, many differing in end-cap structures, can be derived from a glycol radical enzyme-associated microcompartment. The range of pleomorphic shells observed, which span ≈ 2 orders of magnitude in size from ≈ 25 nm to ≈ 1.8 μ m, reveal the remarkable plasticity of BMC-based biomaterials. In addition, new capped nanotube and nanocone morphologies are observed that are consistent with a multicomponent geometric model in which architectural principles are shared among asymmetric carbon, viral protein, and BMC-based structures.

1. Introduction

Bacterial microcompartments (BMCs) are self-assembling subcellular organelles consisting of a core of catabolic (metabolosomes) or anabolic (carboxysomes) enzymes surrounded by a shell composed of hexameric (BMC-H), trimeric (BMC-T), and pentameric (BMC-P) proteins.^[1] When expressed in the absence of their native enzymatic cargo, BMC shell proteins and their engineered derivatives self-assemble into an array of higher-order structures, including 2D hexagonal sheets,^[2,3] small prolates,^[4,5] open-ended nanotubes,^[2,6–8] dodecahedra,^[9] icosahedra with diameters up to 40 nm,^[4,10–14] and irregular polyhedra.^[8,11,15] The building blocks of these genetically tractable BMC-based biomaterials are structurally redundant, forming either hexagons (BMC-H and BMC-T)^[16,17] or pentagons (BMC-P).^[18] Nonetheless, shell protein

B. H. Ferlez^[+], H. Kirst, M. Sutter, C. A. Kerfeld
MSU-DOE Plant Research Laboratory
Michigan State University
East Lansing, MI 48824, USA
E-mail: msutter@lbi.gov; ckerfeld@lbi.gov

B. H. Ferlez^[+], C. A. Kerfeld
Department of Biochemistry and Molecular Biology
Michigan State University
East Lansing, MI 48824, USA


H. Kirst, M. Sutter, C. A. Kerfeld
Environmental Genomics and Systems Biology and Molecular Biophysics
and Integrative Bioimaging Divisions
Lawrence Berkeley National Laboratory
Berkeley, CA 94720, USA

B. J. Greber^[++], E. Nogales
California Institute for Quantitative Biosciences (QB3)
University of California, Berkeley
Berkeley, CA 94720, USA

B. J. Greber^[++], E. Nogales
Molecular Biophysics and Integrative Bioimaging Division
Lawrence Berkeley National Laboratory
Berkeley, CA 94720, USA

E. Nogales
Howard Hughes Medical Institute
University of California, Berkeley
Berkeley, CA 94720, USA

E. Nogales
Department of Molecular and Cell Biology
University of California, Berkeley
Berkeley, CA 94720, USA

 The ORCID identification number(s) for the author(s) of this article can be found under <https://doi.org/10.1002/adma.202212065>

[+] Present address: Department of Molecular Biology and Genetics, Cornell University, Ithaca, NY 14853, USA

[++] Present address: Division of Structural Biology, The Institute of Cancer Research, London SW7 3RP, UK

© 2023 The Authors. Advanced Materials published by Wiley-VCH GmbH. This is an open access article under the terms of the Creative Commons Attribution-NonCommercial-NoDerivs License, which permits use and distribution in any medium, provided the original work is properly cited, the use is non-commercial and no modifications or adaptations are made.

DOI: 10.1002/adma.202212065

paralogs are functionally diverse, with surfaces, pores, and interfaces that reflect the permeability, encapsulation, and assembly of their respective native organelles.

The propensity for synthetic BMC architectures to self-assemble in the absence of their native cargos in vivo and in vitro,^[19] as well as their plasticity for accommodating structural modifications,^[20–23] make them attractive targets for synthetic biologists and bioengineers aiming to confine and coordinate chemistries with precise spatial control.^[24] However, only a few examples of synthetic metabolosome shell systems have been characterized to date, with isolation procedures typically involving differential centrifugation. These include shells derived from B₁₂-dependent 1,2-propanediol utilizing (PDU)^[8] or ethanolamine utilizing BMCs,^[15] a BMC of unknown function from *Haliangium ochraceum* (HO),^[14] and, more recently, a choline-metabolizing glycol radical enzyme-associated micro-compartment (GRM2) from *Klebsiella pneumoniae*.^[11] This limited complement of characterized systems stands in stark contrast to our growing appreciation of the natural abundance and diversity of BMCs, with 68 subtypes now identified in ≈20% of bacterial genomes spanning 45 phyla.^[25] However, this dichotomy between experimentally characterized and bioinformatically-identified BMCs represents an opportunity to expand our portfolio of building blocks, as well as advance our understanding of the molecular mechanisms governing their self-assembly to inform the design of sustainable bio-based architectures for drug delivery, cell-free synthesis, metabolic engineering, and bioelectronics.

In this work, we set out to expand the repertoire of characterized synthetic metabolosome BMC shell chassis by applying the complementation-based affinity purification (CAP) method^[20] to rapidly isolate heterologously assembled shells derived from the B₁₂-independent 1,2-propanediol metabolizing GRM3C organelle from the purple non-sulfur bacterium *Rhodospseudomonas palustris* BisB18.^[25,26] The building block set of this shell system is composed of four distinct types of hexamers, a trimer, and a pentamer. The synthetic GRM3C architectures produced from a self-assembling mixture of these 6 types of proteins are morphologically diverse, some evoking parallels to single walled carbon nanotubes and mature HIV-1 capsids. These structures span the nano- to microscale, and serve as an exemplar for the remarkable structural plasticity of BMC-based biomaterials. Moreover, we propose that pleomorphic capped nanotubes and nanocones that we observed reflect an underlying geometric organization of hexagon and pentagon shell proteins analogous to the 6- and 5-member carbon rings of fullerenes, in which the asymmetrical distribution of the pentamers influences morphology. Our results suggest the existence of shared architectural principles among asymmetric carbon, viral protein, and BMC-based architectures.

2. Results and Discussion

2.1. Operon Design

The native GRM3C locus in *R. palustris* BisB18 encodes a total of six shell proteins: Four hexameric BMC-H paralogs (pfam00936), one pseudo-hexameric trimer BMC-T (2xpfam00936), and one pentameric BMC-P (pfam03319). Our synthetic GRM3C operon

encodes all six of these shell proteins under the control of a T7 promoter (Figure 1).

BMC-P shell proteins are defining elements of BMC loci^[25,30] and despite their low numerical abundance relative to hexagonal shell protein building blocks (BMC-H and BMC-T), they play an important structural role by sealing the vertices of a polyhedral BMC shell.^[18,31,32] The ubiquity of BMC-P across functionally diverse BMC types, coupled with reports demonstrating that incorporation of a Strep Tag II modified BMC-P homolog enabled rapid purification of both empty synthetic metabolosome^[20] and β -carboxysome shells,^[4] led us to hypothesize that this affinity purification strategy could be used to isolate synthetic GRM3C shells assembled heterologously in *Escherichia coli*. To that end, we added a (Gly-Ser)₂ linker and the 8-amino-acid Strep Tag II sequence to the C-terminus of the only BMC-P shell protein encoded in our synthetic operon as a handle to isolate empty GRM3C shells using CAP.^[20]

2.2. Purification of Structurally Diverse Synthetic GRM3C Shells

To identify the shell proteins in our purified GRM3C sample, concentrated eluate from a StrepTrap affinity column was analyzed by SDS-PAGE and mass spectrometry (Figure 2A). Bands 1 and 2 both contain a mixture of BMC-H₁ (9.6 kDa), BMC-H₃ (9.4 kDa), and BMC-H₄ (10.7 kDa). As expected, we also observed BMC-P_{strep} (10.2 kDa) in Band 2. Band 3 contained the remaining two shell proteins, BMC-T (27.4 kDa) and BMC-H₂ (18.7 kDa). Two additional gel fragments spanning the 15–20 kDa range (where we expected BMC-H₂ to migrate based on its predicted molecular weight) were also excised for mass spectrometry analysis and provided evidence of low amounts of BMC-H₂, BMC-T, as well as, some possible BMC-H₁, BMC-H₃, and BMC-H₄ dimers not completely disassembled in the reducing SDS sample buffer (Table S2, Supporting Information). Next, we measured the relative abundance of the six shell proteins in concentrated eluates from independent purifications using mass spectrometry. The amount of each shell protein from three biological replicates was averaged and normalized relative to the BMC-P_{strep} content. The ratio of GRM3C shell proteins in our StrepTrap purified samples was 1.2 ± 0.2 (BMC-H₁):0.4 ± 0.1 (BMC-H₂):1.1 ± 0.2 (BMC-H₃):0.5 ± 0.1 (BMC-H₄):0.9 ± 0.1 (BMC-T):1.0 ± 0.2 (BMC-P_{strep}), or when all four BMC-H proteins are combined, 3.2 ± 0.3 (BMC-H_{1–4}):0.9 ± 0.1 (BMC-T):1.0 ± 0.2 (BMC-P_{strep}) (Table S3, Supporting Information). The successful identification of all six shell proteins in the StrepTrap eluate, coupled with the abundance of untagged hexagonal building blocks (BMC-H and BMC-T) relative to BMC-P_{strep}, suggests higher-order interactions between shell proteins and is consistent with the self-assembly of synthetic shells. Due to the use of the BMC-P_{strep} as an affinity purification handle, the abundance of this protein is higher than expected from the observed structures since it includes some protein that is not incorporated into assemblies. At the same time, any structures formed that do not include a BMC-P subunit, such as previously observed 2D hexagonal sheets^[2,3] or open-ended nanotubes,^[2,6–8] would not be captured.

To confirm the assembly of GRM3C shells, we examined the StrepTrap eluate containing all six shell proteins using dynamic light scattering (DLS) and negative-stained electron mi-

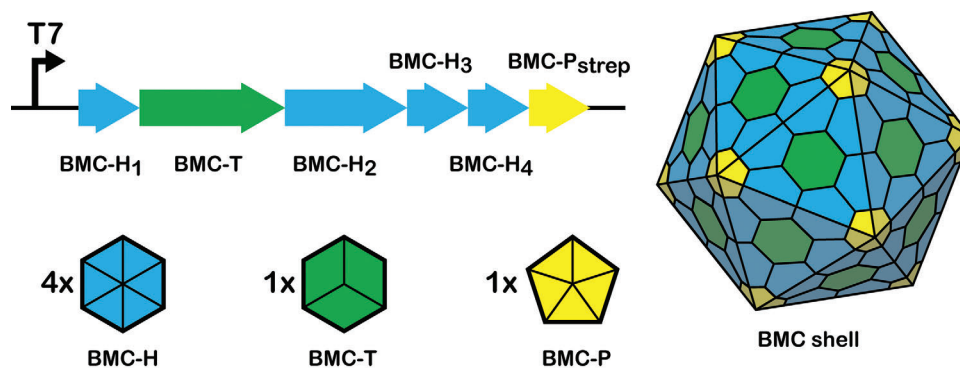


Figure 1. GRM3C shell proteins and design of the synthetic operon. All six genes encoding shell proteins in the GRM3C locus from *R. palustris* BisB18 are expressed in *E. coli* under the control of a T7 promoter. The Ribosome binding site (RBS) preceding BMC-H₁ is derived from pET29b.^[27] Native RBS sequences were used for BMC-T, BMC-H₂, and BMC-H₃ by including the intergenic sequences upstream of each gene in the *R. palustris* BisB18 genome. A synthetic RBS^[28] and intergenic region from *Synechocystis* sp. PCC 6803 were used preceding BMC-H₄ and BMC-P_{strep}, respectively. Due to a ≈ 100 amino acid C-terminal extension, BMC-H₂ is almost twice the length as BMC-H_{1,3}. We modified the native BMC-P sequence to include a C-terminal Strep Tag II sequence for purification (BMC-P_{strep}). The shell proteins can be further classified into clades relative to all identified BMC shell protein sequences: BMC-H₁: H_robinEggBlue, BMC-H₂: H_pumpkin, BMC-H₃: H_tan, BMC-H₄: H_p_GrpU_ickyGreen, BMC-T: Tsp_turquoiseBlue, BMC-P: P_stone according to the classification of Sutter et al.^[25] and Melnicki et al.^[29]

scopy (EM). The DLS profile of our GRM3C sample shows a broad distribution of particle sizes ranging from ≈ 30 to 200 nm (Figure 2B). Electron microscopy images collected after sample dehydration and staining with uranyl acetate confirmed the presence of shells and reveal a remarkably diverse array of morphologies (Figure 2C). In addition to small ≈ 25 –30 nm symmetric particles (Figure 2C, black arrow) similar in appearance to synthetic icosahedral shells from other systems,^[4,10,11] we also observed larger, irregular polyhedra ≈ 100 –200 nm in diameter reminiscent of native BMCs (Figure 2C, yellow arrow).^[33,34] Furthermore, GRM3C shells also appeared to form both capped nanotubes (Figure 2C, cyan arrow) as well as ovoid structures with regions of sharp curvature (Figure 2C, magenta arrow). Interestingly, we also observed examples of nested shells, with one or more smaller shells encapsulated within a larger polyhedron (Figure 2C, white arrow), similar to those reported previously.^[5] These results demonstrate that the CAP method can successfully isolate shells of drastically different sizes and shapes, including the unique capped nanotubes and ovoid morphologies that had not been characterized previously.

We undertook Cryo-EM analyses of GRM3C synthetic shell samples to substantiate the pleomorphic distribution of shell assemblies observed with negative-stained EM, including populations of small spherical particles (Figure 2D, black arrow), large irregular polyhedra (Figure 2D, yellow arrow), ovoids (Figure 2D, magenta arrow), and capped nanotubes (Figure 2D, cyan arrow). Furthermore, a range of different cap morphologies are also observed in our cryo-electron microscopy images (Figure 2D), confirming the diversity seen with negative-stained EM.

2.3. Structural Characterization and Modeling of GRM3C Icosahedra

Because of our purification method, all GRM3C shells observed, including the icosahedral shells, are expected to incorporate BMC-P_{strep}, the only BMC-P shell protein encoded within our

synthetic operon. On the other hand, the presence and relative abundance of the five hexagonal shell proteins (BMC-H_{1,4} and BMC-T) within each of the different shell morphologies remains an open question. In the cryo-EM structures of the two icosahedral GRM3C shells we obtained (Figure S1, Text S1, Supporting Information), the pentamers are, as expected, in the vertex positions. However, we could not distinguish the different hexagonal BMC-H and BMC-T building blocks of the facets. The cryo-EM maps of $T = 4$ and $T = 7$ shells are best fit by BMC-H₁, a member of the basal hexamer shell protein clade, which are typically the major components of functionally diverse shell systems.^[25,29] However, the resolution of our data does not allow us to confidently distinguish between BMC-H₁, BMC-H₂, and BMC-H₃. Therefore, shells likely contain a mixture of BMC-H components with varying positions within the shell. Additionally, BMC-H₃ has 77% sequence identity to BMC-H₁ and, like BMC-H₂ (53% identical to BMC-H₁ when comparing their BMC domains), shares similar interface and pore motifs with BMC-H₁ (Figure S2, Supporting Information). We did not detect any evidence for the ≈ 100 amino acid C-terminal extension of unknown function of BMC-H₂ in our shell structures, in agreement with a PONDR^[35] analysis predicting this sequence to be disordered. BMC-H₁ and BMC-H₃, the most abundant shell proteins in our purified GRM3C shell samples, are present in roughly equal amounts, indicating that, in addition to their incorporation into these smaller icosahedra, they likely also contribute to the formation of the larger GRM3C shells.

2.4. Structural Characterization and Modeling of Capped GRM3C Nanotubes

2.4.1. Comparison of Capped GRM3C to Open-Ended Bacterial Microcompartment-Hexameric Based Nanotubes

When expressed heterologously in the absence of other shell proteins, some BMC-H homologs self-assemble into

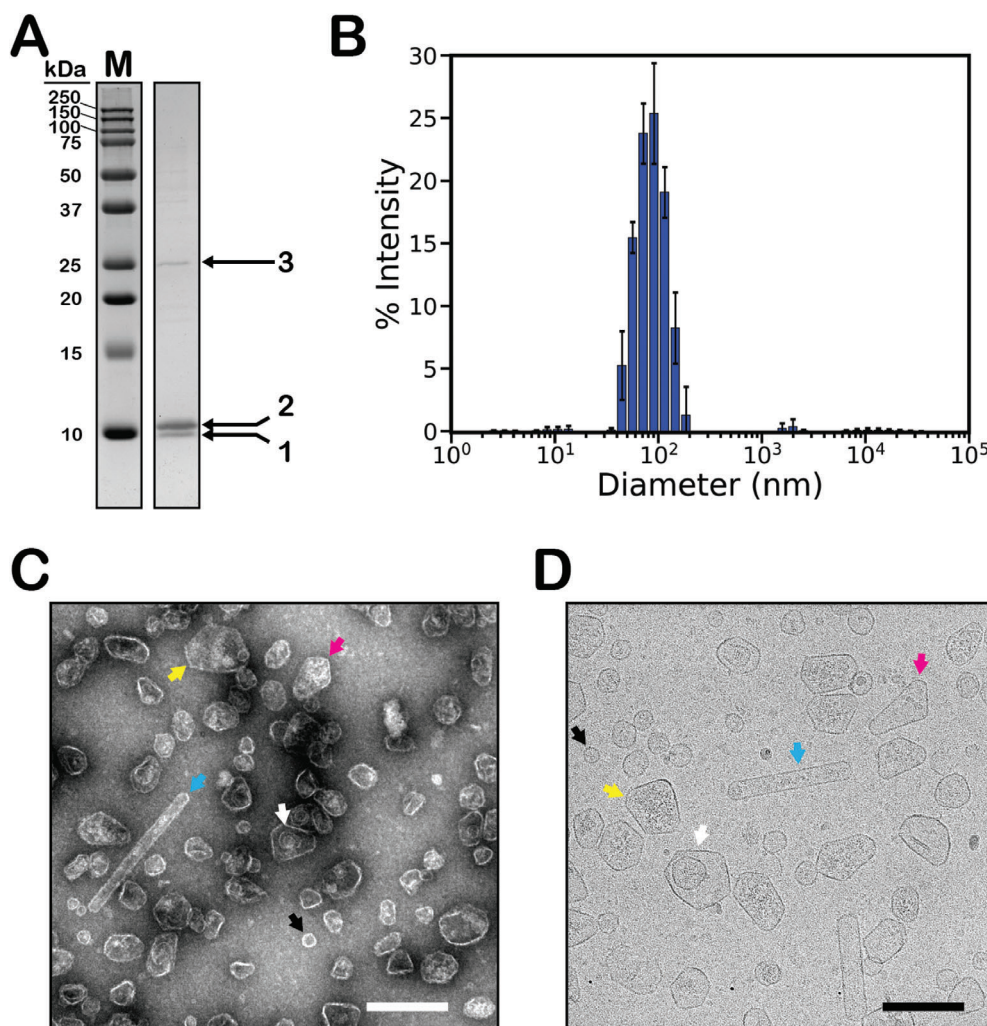


Figure 2. Composition, size, and morphology of synthetic GRM3C shells. A) Coomassie-blue-stained SDS-polyacrylamide gel of concentrated StrepTrap eluate containing GRM3C shell proteins expressed in *E. coli* BL21 (DE3). Numbered bands were analyzed by mass spectrometry. B) Hydrodynamic diameter of purified GRM3C particles measured by dynamic light scattering (DLS). Data represent the average and standard deviation of three measurements. C) Negative-stained and D) cryo electron microscopy images of GRM3C shells. The arrows indicate examples of different shell morphologies: small spheres (black), irregular polyhedra (yellow), nanotubes (cyan), ovoids (magenta), and nested shells (white). Scale bars: 200 nm.

single-component nanotubes $\approx 18\text{--}20$ nm in diameter that can exceed $1\ \mu\text{m}$ in length.^[2,6,7] A BMC-T^{sp}-type^[25] trimer, PduB, has also been reported to assemble into similar, albeit wider, nanotubes with diameters of ≈ 63 nm.^[6] However, none of the previously reported BMC-based nanotubes form closed shells. Instead, they have been conceptualized as the product of rolling a 2D hexagonal array of either BMC-H and/or BMC-T into an open-ended 3-D cylinder in a manner analogous to the rolling of a sheet of graphene into a single-walled carbon nanotube (SWCNT).^[6,7,36] In this model, depending on how the hexagonal lattice is rolled up, the orientation of individual hexagons relative to the longitudinal axis of the resulting tube changes will result in either an armchair, zig-zag, or chiral arrangement (Figure S3, Supporting Information). A similar tiling of BMC-H and BMC-T likely also explains the cylindrical bodies of GRM3C nanotubes. Notably, the GRM3C BMC-T and BMC-H₁ and BMC-H₃ paralogs are closely related to the known open-ended nanotube-forming

shell proteins PduB, PduA, and PduJ, respectively^[29,6] (Table S1, Supporting Information).

Unlike the previously described BMC-based nanotube forming systems, the nanotubes observed in GRM3C shell samples appear to be closed shells, with curved end caps terminating their cylindrical bodies. These unique capped nanotubes span more than an order of magnitude in length, with 56% (272/489) of nanotubes between 51 and 121 nm long, and the remaining 44% (217/489) ranging from 121 nm up to $\approx 1.8\ \mu\text{m}$ (Figure 3A). Moreover, the frequency of long tubes may be underestimated, given that even the mild centrifugation ($15\ 000g$ for 5 min) and filtration ($0.45\ \mu\text{m}$) steps used during the CAP purification could feasibly remove some of these extremely large species prior to the affinity chromatography step. In contrast to the broad distribution of observed lengths, the vast majority (89%, 439/489) of nanotubes have diameters between 25 and 50 nm (Figure 3B). Preparation of the negatively stained samples leads to flattening or collapse

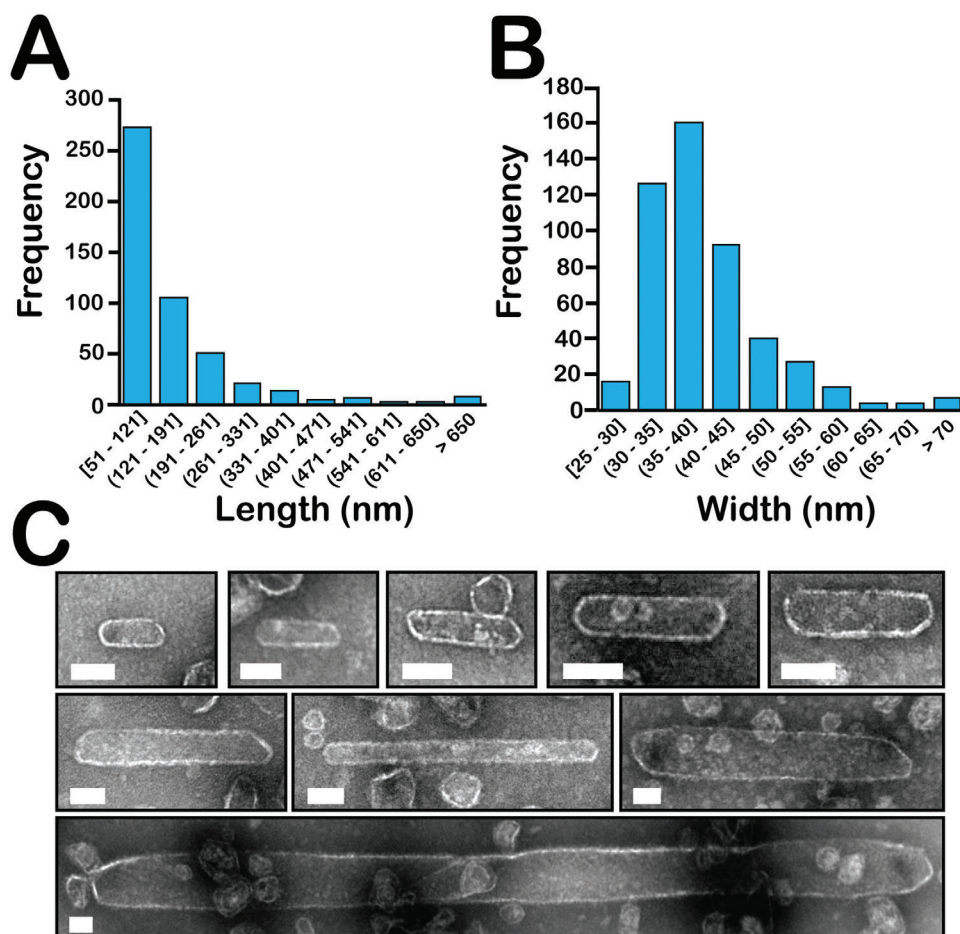


Figure 3. Negative-stained EM characterization of capped GRM3C nanotubes. A) Frequency of observed nanotube lengths and B) widths measured from negative-stained EM images; $n = 489$. Widths represent the average of 2–5 measurements per nanotube. Round brackets are exclusive and square brackets are inclusive. C) Negative-stained EM images showing GRM3C nanotube diversity. Scale bars: 50 nm.

of the nanotubes and can affect their apparent diameter. However, our cryo-EM images (**Figure 4**) show that nanotube diameter ranges that are very similar to the negative stained samples.

2.4.2. Structural Diversity of Nanotube End Caps

Although the geometry of the cylindrical body of a GRM3C nanotube can be explained by the rolling-up of a 2D hexagonal array of shell proteins like open-ended BMC-H or BMC-T nanotubes, the observation of end-capped nanotubes in our electron microscopy images (**Figure 3C**), and the involvement of BMC-P_{strep} (selected for by our affinity-based purification method), points to important differences in their structures and underlying assembly principles. Reports of smaller, ≈ 20 –40 nm long, prolate BMC shells derived from β -carboxysome^[4] and GRM2^[5,11] model shells provide some insight into how the end caps can be formed by analogy to those described for carbon nanotubes.^[37] For example, BMC-H and BMC-P can close a cylindrical tube made of hexagonal shell proteins by splitting an icosahedron into two equal halves, with the circumference of the icosahedron dictating the nanotube diameter, and a variable number of hexamer

belts inserted between the caps, dictating the nanotube length. For the β -carboxysome, there is one hexamer belt between icosahedral hemispheres,^[4] whereas GRM2 shells have been observed with 1 to 4 belts of BMC-H.^[5,11] Despite their substantially shorter lengths compared to the GRM3C nanotubes, the end caps sealing these short prolates can theoretically be used to close a tube of any length. This geometric model has also been used as a framework for interpreting the structures of a number of short prolate viral capsids,^[38] as well as elongated (≈ 50 –100 nm) alfalfa mosaic virus (AMV) nanotubes.^[39] However, the GRM3C BMC proteins are capable of forming end capped BMC nanotubes of up to 1 μm in length, vastly longer than those seen in any previous studies. Furthermore, in stark contrast to end caps derived from bisected icosahedra, GRM3C end caps appear to vary dramatically in their apparent symmetry, and different caps are often observed at opposite ends of the same tube (**Figures 3C and 4A,B**) suggesting a not yet observed plasticity in BMC end cap formation.

Consistent with the heterogeneity observed in GRM3C nanotube caps, we did not identify a subpopulation of nanotubes amenable to structural determination from our cryo-EM data. However, our analyses generated 11 discrete class averages of ≈ 70 nm-long segments of cylindrical nanotube bodies

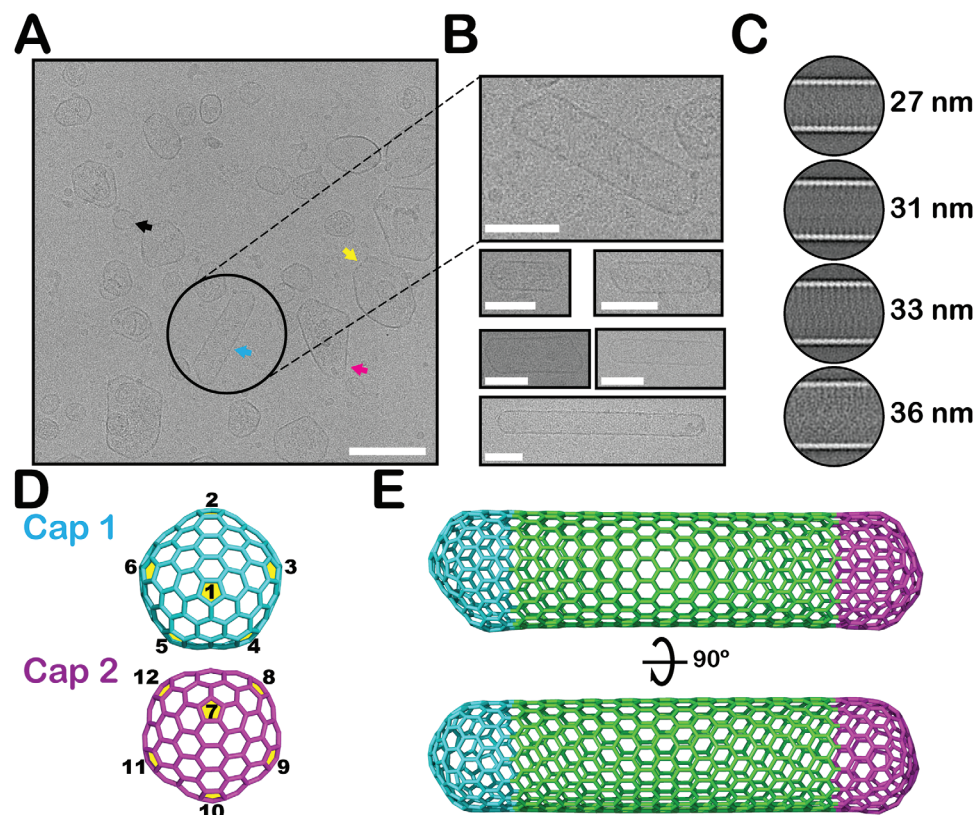


Figure 4. Cryo-EM characterization and geometric model for GRM3C nanotubes. A) Representative cryo-electron microscopy image of purified synthetic GRM3C shells. The arrows indicate examples of different shell morphologies: small spheres (black), irregular polyhedra (yellow), nanotubes (cyan), and ovoids (magenta). Scale bar: 100 nm. B) Examples of nanotube heterogeneity observed by cryo-EM; the top panel, an enlargement from (A), shows a nanotube ≈ 135 nm long, with a diameter of ≈ 36 nm. Scale bars: 50 nm. C) Four class averages of cylindrical nanotube cross sections 27, 31, 33, and 36 nm in diameter. For additional class averages see Figure S4, Supporting Information. D) End-on view of computational models of two example fullerene caps. The distribution of their six respective pentagons (yellow, numbered 1–6 and 7–12) are defined according to the nomenclature of Lair et al.:^[37] 5-2d, 3a (Cap 1, cyan), and 6-0a, 2e (Cap 2, magenta). E) Two orientations of a fullerene-based model of a GRM3C nanotube incorporating the two caps in (D). The zig-zag (16,0) nanotube cylinder is 16 hexagons in circumference and 20 hexagons long, corresponding to a diameter of ≈ 36 nm and length of ≈ 140 nm if constructed from hexagonal BMC-H shell proteins with a side length of 4 nm.

(Figure 4C, Figure S4, Supporting Information). In some classes, a repeating unit of ≈ 3.2 nm in length is observed that roughly corresponds to half the diameter of the hexagonal shell building blocks (i.e., hexameric BMC-H and trimeric BMC-T). Four representative class averages for nanotubes of 27, 31, 33, and 36 nm in diameter are shown in Figure 4C (see Figure S4, Supporting Information, for additional class averages). These averages show that the walls of GRM3C nanotubes are ≈ 3.9 nm thick, and therefore likely constructed, as expected, from a single layer of shell proteins (a single BMC-H or BMC-T shell protein is ≈ 3 nm thick^[12]).

2.4.3. Geometric Models for Capped Bacterial Microcompartment Nanotubes

According to Euler's theorem, additional hexagons and exactly 12 pentagons (six in each cap) are required to close a SWCNT.^[37] One way to satisfy these conditions is to generate end caps by bisecting an icosahedron, as is the case for the synthetic prolate β -carboxysome and GRM2 shells, viral capsids, or the elongated

AMV particles discussed above. Such icosahedron-derived caps could theoretically explain some of the more rounded, symmetric ends of the GRM3C nanotubes, and would be in line with the propensity for BMC shell proteins to form icosahedral shapes when expressed heterologously.^[4,11,12] As noted above, GRM3C shell proteins also assemble into icosahedra with diameters of ≈ 25 nm ($T = 4$) and ≈ 31 nm ($T = 7$) (Figure S1, Supporting Information). Short prolates, albeit at much lower abundance (183 particles vs a total of 4012 for spherical shells), are also formed (Figure S5A, Supporting Information, top right corner). However, a model where caps are derived only from icosahedral hemispheres fails to fully explain the observed morphological diversity in our sample, and why, for example, in the case of GRM3C nanotubes with a diameter matching the ≈ 31 nm circumference of our $T = 7$ icosahedron (Figure 4C), we did not identify a homogenous subpopulation of symmetric caps, further strengthening the concept of end cap plasticity.

If we allow for more flexibility in the spatial distribution of the six pentamers per end cap, the potential to create a wide variety of end cap isomers capable of closing a nanotube with a given diameter increases dramatically and allows for the formation of

asymmetric end cap shapes reminiscent of those observed in our GRM3C nanotubes. These fullerene end caps have been extensively characterized in the context of SWCNTs,^[37,40] and depending on the arrangement of pentagons, can seal armchair, zigzag, or chiral hexagonal cylinders (Figure S3, Supporting Information). Following the systematic classification of Lair et al.,^[37] SWCNT end caps can be constructed from the perspective of a base shape at the pole of the cap, either a pentagon (in our case, BMC-P) or hexagon (in our case, BMC-H or BMC-T), with the relative positions of the remaining 5 (or 6) pentagons determining the final shape and circumference of the nanotube. The ability of GRM3C nanotubes to incorporate diverse, asymmetric fullerene-based end caps could therefore explain their underlying structural heterogeneity, especially when we consider that two different end caps, with unique distributions of pentagons and relative orientations, can seal opposite ends of the same tube.

This geometric model can recapitulate the observed heterogeneity of GRM3C nanotubes. We constructed a fullerene nanotube with two different end caps in silico, one with a pentagon (Figure 4D, Cap 1) and the other a hexagon base plate (Figure 4D, Cap 2). A nanotube model incorporating these two example caps (Figure 4E), viewed perpendicular to its longitudinal axis to imitate the orientation of GRM3C nanotubes in our EM images, closely resembles our empirically observed morphologies (see, for example, Figure 4B, top). Moreover, rotating this model by 90° highlights the angular dependence of the apparent asymmetry of the end caps (in particular, Cap 1). How a nanotube is deposited on a negative-stained EM grid, or oriented in vitreous ice for cryo-EM, could therefore potentially obscure characterization of structural heterogeneity during visual inspection. Importantly, our observations of elongated capped nanotubes also bear striking resemblance to a sub-population of elongated BMC architectures observed in a recent computational study.^[41] Although these simulations contained only hexagonal shell components, and explicitly account for the presence of cargo molecules, the simulated architecture contains 12 pentameric defects consistent with both our geometric model and biochemical evidence for incorporation of BMC-P_{strep} within the GRM3C nanotubes.

2.5. Structural Characterization and Modeling of GRM3C Nanocones

Our proposed geometric model for capped BMC nanotubes suggests plasticity in the interactions between BMC-H, BMC-T, and BMC-P, consistent with their ability to assemble into irregular polyhedra. Moreover, our model can explain the formation of other regular fullerene-based architectures such as nanocones, that also have an asymmetric distribution of pentagon subunits. At its apex, a fullerene cone is like the nanotube end cap, except less than 6 pentagons (P) are incorporated before a helical propagation of hexagons extends toward its base. In accordance with Euler's theorem, the base of the cone can also be closed with a multitude of structurally unique end caps containing (12-P) pentagons. The ovoid-shaped GRM3C shells (Figures 2C and 4A, magenta arrows) are consistent with this fullerene-based nanocone model. These GRM3C nanocones, observed in both negative-stained and cryo-EM images (Figure 5A), range in length between 58 and 280 nm, and 98% of particles are between 58

and 175 nm (211/216) (Figure 5B). Apex angles measured from negative-stained EM images further support a conical geometry, and follow a bimodal distribution with modes at 29° and 57°, consistent with the narrowest two theoretical angles of a cone constructed from a hexagonal array (i.e., 30°, 60°) (Figure S6, Supporting Information).^[42] While the negative stain process can slightly affect the morphology due to flattening or collapse of the walls we see the same morphologies in our cryo-EM images (Figure 5A) so a substantial deviation of the measured angles can be excluded. Rare observations of hybrid nanocone-nanotube structures, where it appears the hexagonal extension of a cone's apex takes on a constant curvature resulting in the formation of a nanotube, further supports a common helical arrangement of BMC-H/-T shell proteins in both morphologies (Figure S7, Supporting Information).

The GRM3C nanocones observed in our analyses evoke EM images of mature HIV-1 capsids.^[42,43] Functionally and evolutionarily unrelated to BMC proteins, the HIV-1 capsid is assembled from a single two domain subunit that can oligomerize into either hexamers or pentamers.^[44] In its mature form, these quasi-equivalent building blocks assemble into fullerene cones ≈100 nm in length.^[42,45] When assembled in vitro, HIV-1 capsid proteins can also readily form nanotubes.^[42] By leveraging the decades of detailed biophysical studies of the mature HIV-1 capsid, culminating in atomic-level structures outlining the arrangement of hexagonal and pentagonal subunits,^[43] we propose an analogous geometric model to interpret the structures of GRM3C nanocones (Figure 5C). Consistent with the observed morphological diversity of both the HIV-1 and GRM3C architectures, the proposed conical model, like other fullerenes, can vary dramatically in both size (depending on the number of hexagons) and shape (depending on the distribution of the 12 pentagons at the apices and end caps). In contrast to the HIV-1 capsid, which is formed by a single protein protomer that can assemble into hexagons and pentagons, and even switch between the two conformations,^[43,46,47] BMCs have dedicated proteins forming pentagons (BMC-P) or hexagons (BMC-H/-T). This difference in the architecture of these proteinaceous nanocones likely has consequences of material properties, like rigidity and strain resistance, which must contribute to their distinct functions in biology.

3. Conclusions

Although a comprehensive understanding of the determinants of BMC shell assembly remains enigmatic, recent computational studies have successfully reproduced many of the complex irregular polyhedral shapes observed empirically.^[41,48–50] These reports have highlighted how the relative abundance, absolute concentration, interaction strength, and flexibility of shell proteins, as well as the presence of cargo, can impact the size and shape of a BMC shell. The insights from these computational studies, coupled with the conservation of common interface motifs between BMC-H and BMC-P shell proteins, suggest a molecular explanation for the pleomorphic diversity of GRM3C shells that likely involves multiple factors, including intrinsic properties of the individual subunits, their abundance, as well as their spatial distribution within the shell. Given the multiple distinct hexamers and the pseudohexamer present in our assembly mixture,

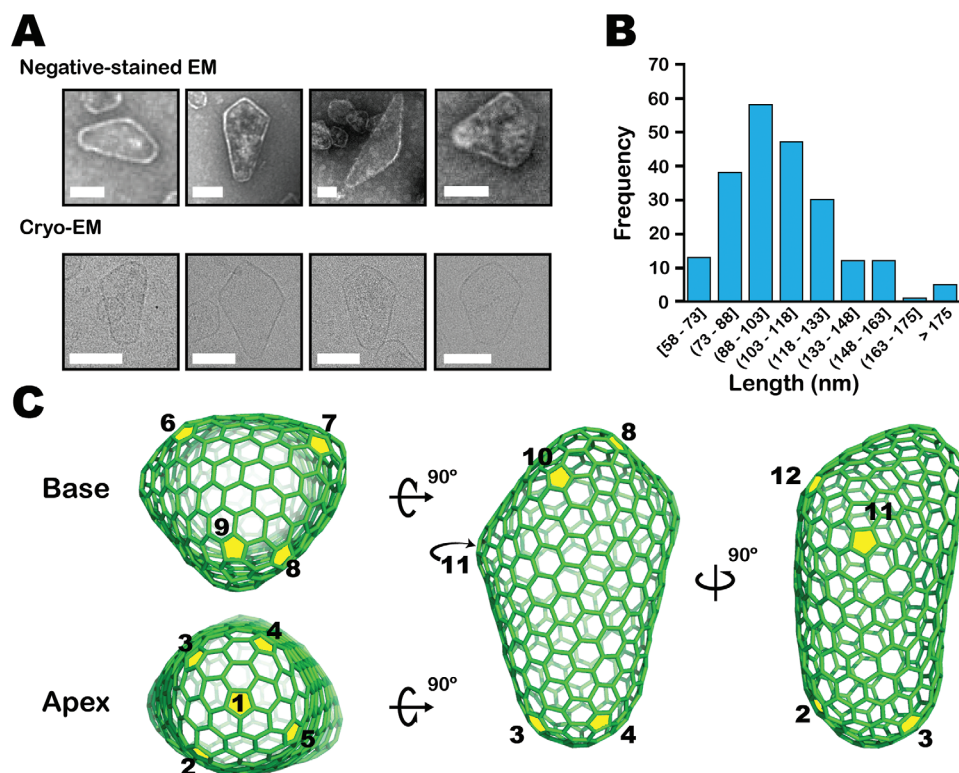


Figure 5. EM characterization and geometric model of GRM3C nanocones. A) Examples of nanocones from purified GRM3C samples imaged by negative-stained (top) or cryo-EM (bottom). Scale bars: 50 nm. B) Distribution of nanocone lengths measured from negative-stained EM images ($n = 216$). Round brackets are exclusive and square brackets are inclusive. C) A geometric model of a fullerene cone derived from the atomic-level structure of a mature HIV-1 capsid (PDB ID: 3J3Q)^[43] composed of 216 hexagons and 12 pentagons (yellow, numbered). When built with BMC shell proteins, this model corresponds to a nanocone of about 75 nm in length.

it is reasonable to assume that the different morphologies observed result from different hexamer lattice compositions, and that these may vary in flexibility to accommodate local curvature introduced by the pentamers/end caps; this would alter the frequency with which pentamers are incorporated into the hexagonal lattice. To test this hypothesis, systematically characterizing the structural diversity formed by specific combinations of shell proteins, is a fundamental next step in developing BMC shell proteins into a platform technology for predictive building of nanocompartments and microcompartments for a range of applications in biomedicine and bioengineering. Indeed, being able to predictably construct nanocontainers of defined size, shape, and charge is not only important for compartmentalizing metabolic pathways, but is critical for other potential applications of shells, including those involving uptake by cellular targets and cargo delivery. In this context, icosahedral particles previously characterized are of limited size (20–40 nm). The larger compartments described here may be better suited for cargo delivery applications; for example, packaging DNA or RNA molecules into the capsid-like nanocone shell.

Despite recent advances in BMC shell protein engineering, the number of synthetic metabolosome shell systems that have been experimentally characterized remains limited. The rapid isolation of pleomorphic shells from a new synthetic GRM3C system that span almost two-orders of magnitude in size from 25 nm to $\approx 1.8 \mu\text{m}$ shows that we have only begun to explore the functional

and structural potential of this remarkable self-assembling and genetically tractable biomaterial. In addition to shapes observed previously, such as small symmetric icosahedra and large irregular polyhedra, GRM3C shell proteins also form regular, yet asymmetric, capped nanotube and nanocone architectures that incorporate BMC-P. The heterogeneity of these new shapes is consistent with a model based on the hexagon and pentagon composition of fullerenes, and suggests that common geometric principles underlie the assembly of asymmetric carbon, viral protein, and BMC-based architectures.

4. Experimental Section

Synthetic Operon Design: The six genes encoding shell proteins in the GRM3C locus from *R. palustris* BisB18, referred to in this manuscript as BMC-H₁ (Locus tag: RPC_1165; Uniprot accession: ABD86728), BMC-T (RPC_1166; ABD86729), BMC-H₂ (RPC_1167; ABD86730), BMC-H₃ (RPC_1168; ABD86731), BMC-H₄ (RPC_1175; ABD86738), and BMC-P (RPC_1172; ABD86735), were PCR amplified from *R. palustris* BisB18 genomic DNA (see Table S1, Supporting Information, for amino acid sequences of all proteins). The intergenic region between *cpcB* and *cpcA* was PCR amplified from the *Synechocystis* sp. PCC 6803 genome. The PCR products were cloned into pBbE2K^[27] by Gibson assembly^[51] to form a synthetic operon, in which the *cpcB*-*cpcA* intergenic region served as the intergenic region between BMC-H₄ and BMC-P_{strep} (see Sequence S1, Supporting Information, for complete plasmid DNA sequence) and a synthetic ribosome binding site^[28] was used in front of the BMC-H₄ gene. A flexible

(GlySer)₂ linker and Strep Tag II were added on the C-terminus of BMC-P using Gibson assembly. The amino acid sequences of all shell proteins encoded in the synthetic GRM3C operon are listed in Table S1, Supporting Information.

Growth, Expression, and Purification of Synthetic GRM3C Shells from *E. coli*: Lysogeny broth starter cultures supplemented with 50 μg mL⁻¹ kanamycin were inoculated with *E. coli* BL21(DE3) cells carrying the pBbE2K plasmid containing the synthetic GRM3C operon from *R. palustris* BisB18 and grown overnight at 37 °C while shaking at 200 RPM. 10 mL of the starter culture was used to inoculate flasks containing 1 L of lysogeny broth with 50 μg mL⁻¹ kanamycin and the culture shaken at 37 °C and 200 RPM until they reached an OD₆₀₀ of ≈0.6–0.8, at which point protein expression was induced by adding IPTG to a final concentration of 250 μM. After adding IPTG, the temperature was lowered to 18 °C and protein expression allowed to continue overnight while shaking at 200 RPM. Cells were harvested by centrifugation at 8000g for 10 min at 25 °C and resuspended using B-PER detergent lysis reagent (ThermoFischer) supplemented with 1X SigmaFast protease inhibitor (Sigma Aldrich), 2 μL of 50 mg mL⁻¹ lysozyme per ml lysis reagent, and 1 mg DNaseI, at a ratio of 4 mL g⁻¹ of cells according to the manufacturers' guidelines. Unbroken cells were removed by centrifugation at 15 000g for 5 min at 25 °C and the resulting lysate filtered through a 0.45 μm syringe filter before loading onto a 5 mL StrepTrap column equilibrated with a buffer containing 10 mM Tris-HCl pH 8.0 with 300 mM NaCl (Buffer A) at 5 mL min⁻¹ using an Akta Pure FPLC at 10 °C; for GRM3C sample preparations for Cryo-EM, Buffer A was composed of 20 mM HEPES pH 7.4 and 50 mM NaCl. After loading the cell lysate, the column was washed with 5 column volumes of Buffer A before eluting shells with Buffer A containing 2.5 mM desthiobiotin. Pooled StrepTrap elution fractions were concentrated with a 100 kDa MWCO centrifugal filter at 4 °C at 4500g to a final volume of ≈0.5–1 mL. For SDS-PAGE, 15 μL of the concentrated shell sample was mixed with 5 μL of 4X reducing SDS sample buffer and boiled for 10 min before loading onto an SDS-polyacrylamide gel (4% stacking/18% separating).

Mass Spectrometry Sample Preparation, Data Collection, and Analysis Proteolytic Digestion: Gel bands excised from the 18% acrylamide separating gel of purified GRM3C shells were digested in-gel according to Shevchenko et al.^[52] with modifications. Briefly, gel bands were dehydrated using 100% acetonitrile (ACN) and incubated with 10 mM dithiothreitol in 100 mM ammonium bicarbonate, pH ≈ 8, at 56 °C for 45 min, dehydrated again, and incubated in the dark with 50 mM iodoacetamide in 100 mM ammonium bicarbonate for 20 min. Gel bands were then washed with ammonium bicarbonate and dehydrated again. Sequencing grade modified trypsin was prepared to 0.01 μg μL⁻¹ in 50 mM ammonium bicarbonate and ≈100 μL of this was added to each gel band so that the gel was completely submerged. Bands were then incubated at 37 °C overnight. Peptides were extracted from the gel by water bath sonication in a solution of 60% ACN/1% trifluoroacetic acid (TFA) and vacuum dried to ≈2 μL. Dried peptides were then re-suspended in 2% ACN/0.1% TFA to 20 μL prior to injection.

LC/MS/MS Analysis: An injection of 5 μL was automatically made using a Thermo (www.thermo.com) EASYnLC 1000 onto a Thermo Acclaim PepMap RSLC 0.1 mm × 20 mm C18 trapping column and washed for ≈5 min with buffer A. Bound peptides were then eluted over 35 min onto a Thermo Acclaim PepMap RSLC 0.075 mm × 250 mm resolving column with a gradient of 5%B to 40%B in 24 min, ramping to 90%B at 25 min and held at 90%B for the duration of the run (Buffer A = 99.9% water/0.1% formic acid, Buffer B = 80% ACN/0.1% formic acid/19.9% water) at a constant flow rate of 300 nL min⁻¹. Column temperature was maintained at a constant temperature of 50 °C using and integrated column oven (PRSO-V1, Sonation GmbH, Biberach, Germany).

Eluted peptides were sprayed into a ThermoScientific Q-Exactive mass spectrometer (www.thermo.com) using a FlexSpray spray ion source. Survey scans were taken in the Orbitrap (35 000 resolution, determined at *m/z* 200) and the top 15 ions in each survey scan are then subjected to automatic higher energy collision induced dissociation (HCD) with fragment spectra acquired at 17 500 resolution. The resulting MS/MS spectra are converted to peak lists using Mascot Distiller, v2.8.0.1 (www.matrixscience.com) and searched against *R. palustris* BisB18 shell protein sequences and all *E. coli* protein sequences (downloaded 2020-11-

19, www.uniprot.org) appended with common laboratory contaminants (downloaded from www.thegpm.org, cRAP project) using the Mascot searching algorithm, v 2.7. The Mascot output was then analyzed using Scaffold, v5.0.0 (www.proteomesoftware.com) to probabilistically validate protein identifications. Assignments validated using the Scaffold 2% FDR confidence filter and containing 4 unique peptides are considered true. The resulting percent sequence coverage for each GRM3C shell protein is listed in Table S2, Supporting Information. Mascot parameters for all databases were as follows: i) Allow up to 2 missed tryptic sites, ii) fixed modification of Carbamidomethyl Cysteine, iii) variable modification of Oxidation of Methionine, iv) peptide tolerance of ±10 ppm, v) MS/MS tolerance of 0.02 Da, vi) FDR calculated using randomized database search.

Mass Spectrometry Quantification of Relative Shell Protein Abundances: To calculate the relative abundance of each shell protein, biological replicates of purified shells from three independent 1 L cultures were analyzed. Total protein content of reducing SDS-PAGE samples prepared from concentrated StrepTrap eluates (see Section 4: Growth, expression, and purification of synthetic GRM3C shells from *E. coli*) were normalized to an A280 of 0.513 and equal volumes loaded onto a polyacrylamide gel with a 4% acrylamide stacking layer. The gel was run at room temperature for 20 min at 50 V to concentrate the shell samples into a single band within the 4% acrylamide stacking layer. The gel was stained with Coomassie blue and the concentrated band representing the total protein content of each eluate was excised and placed into separate tubes with 100 μL of 5% acetic acid. Samples were proteolyzed and analyzed as described above. The normalized average total ion current (TIC) for each shell protein was quantified using Scaffold, v5.0.0 (www.proteomesoftware.com) as described above, and used to calculate the abundance of each BMC-H and BMC-T shell protein relative to the amount of BMC-P (Table S3, Supporting Information).

Negative-Stained Transmission Electron Microscopy: Uranyl acetate-stained GRM3C shells were imaged using a JEM-1400Flash microscope (JEOL) with a bottom-mounted Matataki Flash sCMOS camera (JEOL). Grids were prepared as described in Ferlez et al.^[21] by floating a carbon-coated copper grid on top of 5 μL of StrepTrap eluate containing GRM3C shells for 30 s, wicking the excess solution away using Whatman paper, followed by floating the grid on top of 5 μL of 1% uranyl acetate for 15 s before removing excess stain with Whatman paper.

Dynamic Light Scattering: DLS data were collected using a Wyatt DynaPro Nanostar. 5 μL of the pooled StrepTrap elution fractions were loaded into a 1 μL cuvette and three scans, each consisting of 20 5 s acquisitions, were used to measure the size distribution of GRM3C shells in solution. The percent scattered light intensity for the three scans were averaged and plotted along with their standard deviation.

Cryo-EM Specimen Preparation and Data Collection: A thin film of continuous carbon (prepared in-house) was floated onto R1.2/1.3 holey carbon grids or UltraAufoil R1.2/1.3 gold foil grids (Quantifoil Microtools). After drying (at least overnight), the grids were plasma cleaned using a Tergeo plasma cleaner (PIE Scientific). 4 μL of GRM3C shell sample at a concentration of 1.5 mg mL⁻¹ were applied to the grid and incubated for ≈30 s in the humidity chamber of a Vitrobot Mk IV (Thermo Fisher Scientific) to allow the particles to adsorb to the carbon film. Subsequently, the liquid was blotted away for 5–7 s and the specimen was vitrified by plunging it into a mixture of liquid ethane and propane at liquid nitrogen temperature.^[53]

The grids were first screened using a Tecnai F20 cryo-transmission electron microscope (FEI) operated at 120 kV acceleration voltage and equipped with a US4000 CCD camera (Gatan). Selected grids were then loaded into a Talos Arctic cryo-transmission electron microscope (Thermo Fisher Scientific) operated at 200 kV acceleration voltage. Data were acquired at 0.5–1.5 μm underfocus using a K3 direct electron detector (Gatan) operated in super-resolution counting mode, with electron microscopy image movies fractionated into 50 frames at a total exposure of 25 electrons Å⁻², and with the microscope set to 35 638× magnification, resulting in a pixel size of 1.403 Å on the object scale (super-resolution pixel size 0.7015 Å). The data collection was automated using SerialEM^[54] and accelerated by using image shift to acquire data in 9 holes per stage position. A total of 1102 movies were recorded, of which 378 were acquired

on one holey carbon grid and 724 on one holey gold grid (both of them carbon-coated, as described above).

Cryo-EM Data Processing: All data processing was performed in RELION 3.0,^[55,56] unless stated otherwise. Beam-induced motion in the electron microscopy image movies was corrected using the CPU-based implementation of motion correction within RELION (movies subdivided into 3×3 patches), followed by CTF parameter fitting using CTFFIND 4^[57] from within RELION. Based on the quality of the CTF parameter fits, 858 aligned and summed movies were retained for further processing.

For the analysis of tubular shell structures from cryo-electron microscopy images, all tubular assemblies were picked manually from 858 selected microscopy images. Particles were extracted at a pixel size of 1.05 Å and a step size of 70 Å along the tube axis. The extracted dataset was subjected to repeated 2D classification to remove tube caps or aberrant particles, such that tubes of different diameters could be resolved in a final round of 2D classification (shown in Figure 3C and Figure S4, Supporting Information). Nanotube wall thickness and overall diameter of GRM3C nanotube class averages were measured with Fiji using a pixel size of 1.05 Å (see Figure S4, Supporting Information, for example measurements).

For reconstruction of symmetrical shells (Figures S1 and S5, Supporting Information), particles with roughly spherical appearance (i.e., putative icosahedral symmetry), were manually picked from a subset of microscopy images because of the extreme heterogeneity of the specimen, and 2D classification was used to generate picking references, notably including shells of different diameters, for subsequent automated selection of a dataset of particles with putative icosahedral symmetry. A total of 90 863 particle coordinates were identified, which included a diverse array of particles, comprising round (i.e., symmetrical or quasi-symmetrical) particles and tips of elongated or tubular structures. The auto-picked particles were subjected to two rounds of 2D classification, initially selecting 6436 spherical, putatively icosahedral, particles of different sizes, and then identifying large and small diameter shell classes (1154 large particles with hexagonal appearance, 1518 large particles with round appearance, 1340 small particles) within those initially-selected particles. Additionally, 183 bullet-shaped, or prolate particles were identified, similar to those observed in other microcompartment systems.^[4,5] However, this subset could not be refined reliably, likely owing to the small number of particles and reduced symmetry. All other classes represented irregular or tubular structures. Refinement of the 1154 large and 1340 small shell particles revealed that they correspond to $T = 7$ (large) and $T = 4$ (small) icosahedral shells. These two particle classes were subsequently processed independently.

For the $T = 7$ shell, the particle subsets with hexagonal and round appearance in 2D classes were initially processed separately. Particles belonging to the classes with hexagonal appearance, which appeared more sharply defined than the round particles of the same diameter, were extracted at their original 1.403 Å pixel size, followed by 3D auto-refinement and CTF refinement (magnification anisotropy, per-particle defocus, beam tilt), 3D auto-refinement, and 3D classification. The best 3D class was again refined and subjected to CTF refinement, resulting in a 3.9 Å-resolution map from 870 particles. The particles belonging to the 2D classes of similar size to the $T = 7$ shell, but with round appearance, were of lower apparent quality (as judged from the resolution of 3D auto-refinements) and were therefore initially 2D-subclassified, 3D auto-refined, and 3D-subclassified using the binned 4.209 Å/pixel particle images. The 431 remaining particles were extracted at the original pixel size (1.403 Å), and subsequently 3D auto-refined, subjected to two rounds of CTF refinement (anisotropic magnification, per-particle defocus, beam tilt), and further refined, resulting in a reconstruction at 4.7 Å resolution. Further 3D classification identified 362 higher-quality particles, which were added to the previously identified 870-particle subset of $T = 7$ shells.

The joined dataset of 1232 $T = 7$ shell particles was refined and CTF refined (per-particle defocus and astigmatism, beam tilt). The dataset was then symmetry expanded with icosahedral (I_2) symmetry (resulting in 73920 particles), which appeared to aid with subsequent CTF refinement (which included per-particle defocus, per-microscopy-image astigmatism, and beam tilt, followed by beam tilt, trefoil and 4th order aberrations). 11 400 particles originating from microscopy images with poor

ice quality (as judged by manual microscopy image inspection) were excluded, resulting in a 3.6 Å resolution reconstruction of the $T = 7$ shell from 62 520 particles (Figure S5A, Supporting Information). For the $T = 4$ shell, 1340 particles were selected and refined using the binned 4.209 Å/pixel data, followed by extraction of unbinned particle images with improved centering quality. The unbinned particles were 3D auto-refined to 4.4 Å resolution. After CTF refinement (magnification anisotropy followed by per-particle defocus and beam tilt), 3D auto-refinement and 3D classification, 1190 high-quality particles were selected. This subset was subjected to two rounds of CTF refinement (per-particle defocus and astigmatism followed by 3D-refinement and refinement of per-particle defocus, per-particle astigmatism, and beam tilt) and 3D-auto refined to 3.5 Å resolution. The dataset was symmetry expanded (resulting in 71 400 particles) and subjected to CTF-refinement (per-particle defocus, per-microscopy-image astigmatism, beam tilt) and refined. Of the 71 400 particles, 57 840 were selected based on microscopy image ice quality (as judged by manual inspection, as above) and refined, resulting in a 3.4 Å resolution reconstruction of the $T = 4$ shell (Figure S5B, Supporting Information). The cryo-EM maps for the icosahedral structures were deposited in the electron microscopy data bank (<https://www.ebi.ac.uk/emdb/>) under accessions EMD-16401 for $T = 4$ and EMD-16402 for $T = 7$.

Nanotube and Nanocone Models: The nanotube model in Figure 3E was built using carbon atoms with optimized molecular geometry in Avogadro 1.2.0.^[58] Two different end caps compatible with a zig-zag nanotube were selected to close a (16,0) graphene nanotube 20 hexagons in length. The distribution of pentagons in each of the two end caps is described following the nomenclature of Lair et al.^[37] Cap 1 is 5-2d,3a and Cap 2 is 6-0a,2e. PyMOL (The PyMOL molecular Graphics System, Version 2.3.4, Schrodinger LLC) was used for visualization and to generate the final image; pentamers were colored using Adobe Illustrator.

The nanocone model in Figure 5C was built with PyMOL by extracting the positions of Ala204 of the HIV-1 proteins from the pdb file 3J3Q,^[43] which is located at the corner position between three subunits, and using those coordinates to draw lines in between them.

Statistical Analysis: Sample sizes for size measurements from electron microscopy images are indicated in the figure legends. A Fourier Shell Correlation curve was used to assess the resolution of the icosahedral $T = 4$ and $T = 7$ structures. Statistical analysis methods for analysis of mass-spectrometry data are detailed in the LC/MS/MS analysis section of the methods.

Supporting Information

Supporting Information is available from the Wiley Online Library or from the author.

Acknowledgements

B.H.F. and H.K. contributed equally to this work. The authors would like to thank Carrie Harwood for providing the culture of *R. palustris* BisB18 and the MSU Metabolomics Center, in particular Douglas Whitten, for both collecting the mass spectrometry data and providing valuable assistance with data analysis. E.N. is a Howard Hughes Medical Institute Investigator. This work was supported by the National Institutes of Health, National Institute of Allergy and Infectious Diseases (NIAID) grant 1R01AI114975-06. Research by C.A.K. and M.S. was supported as part of the Center for Catalysis in Biomimetic Confinement, an Energy Frontier Research Center funded by the U.S. Department of Energy (DOE), Office of Science, Basic Energy Sciences (BES), under award DE-SC0023395.

Conflict of Interest

The authors declare no conflict of interest.

Data Availability Statement

The data that support the findings of this study are openly available in EMDB (the Electron Microscopy Data Bank) at <https://www.ebi.ac.uk/emdb/>, reference number 16401.

Keywords

bacterial microcompartments, fullerenes, nanocones, nanotubes, self-assembly, synthetic biology

Received: December 23, 2022

Revised: March 9, 2023

Published online:

- [1] C. A. Kerfeld, C. Aussignargues, J. Zarzycki, F. Cai, M. Sutter, *Nat. Rev. Microbiol.* **2018**, *16*, 277.
- [2] A. Pang, S. Frank, I. Brown, M. J. Warren, R. W. Pickersgill, *J. Biol. Chem.* **2014**, *289*, 22377.
- [3] M. Sutter, M. Faulkner, C. Aussignargues, B. C. Paasch, S. Barrett, C. A. Kerfeld, L.-N. Liu, *Nano Lett.* **2016**, *16*, 1590.
- [4] M. Sutter, T. G. Laughlin, N. B. Sloan, D. Serwas, K. M. Davies, C. A. Kerfeld, *Plant Physiol.* **2019**, *181*, 1050.
- [5] E. E. Cesle, A. Filimonenko, K. Tars, G. Kalnins, *Protein Sci.* **2021**, *30*, 1035.
- [6] I. Uddin, S. Frank, M. J. Warren, R. W. Pickersgill, *Small* **2018**, *14*, 1704020.
- [7] C. R. Noël, F. Cai, C. A. Kerfeld, *Adv. Mater. Interfaces* **2016**, *3*, 1500295.
- [8] J. B. Parsons, S. Frank, D. Bhella, M. Liang, M. B. Prentice, D. P. Mulvihill, M. J. Warren, *Mol. Cell* **2010**, *38*, 305.
- [9] J. Jorda, D. J. Leibly, M. C. Thompson, T. O. Yeates, *Chem. Commun.* **2016**, *52*, 5041.
- [10] F. Cai, S. L. Bernstein, S. C. Wilson, C. A. Kerfeld, *Plant Physiol.* **2016**, *170*, 1868.
- [11] G. Kalnins, E.-E. Cesle, J. Jansons, J. Liepins, A. Filimonenko, K. Tars, *Nat. Commun.* **2020**, *11*, 388.
- [12] M. Sutter, B. Greber, C. Aussignargues, C. A. Kerfeld, *Science* **2017**, *356*, 1293.
- [13] M. Sutter, S. Mcguire, B. Ferlez, C. A. Kerfeld, *ACS Synth. Biol.* **2019**, *8*, 668.
- [14] J. K. Lassila, S. L. Bernstein, J. N. Kinney, S. D. Axen, C. A. Kerfeld, *J. Mol. Biol.* **2014**, *426*, 2217.
- [15] M. Held, A. Kolb, S. Perdue, S.-Y. Hsu, S. E. Bloch, M. B. Quin, C. Schmidt-Dannert, *Sci. Rep.* **2016**, *6*, 24359.
- [16] C. A. Kerfeld, M. R. Sawaya, S. Tanaka, C. V. Nguyen, M. Phillips, M. Beeby, T. O. Yeate, *Science* **2005**, *309*, 936.
- [17] M. G. Klein, P. Zwart, S. C. Bagby, F. Cai, S. W. Chisholm, S. Heinhorst, G. C. Cannon, C. A. Kerfeld, *J. Mol. Biol.* **2009**, *392*, 319.
- [18] S. Tanaka, C. A. Kerfeld, M. R. Sawaya, F. Cai, S. Heinhorst, G. C. Cannon, T. O. Yeates, *Science* **2008**, *319*, 1083.
- [19] A. R. Hagen, J. S. Plegaria, N. Sloan, B. Ferlez, C. Aussignargues, R. Burton, C. A. Kerfeld, *Nano Lett.* **2018**, *18*, 7030.
- [20] A. Hagen, M. Sutter, N. Sloan, C. A. Kerfeld, *Nat. Commun.* **2018**, *9*, 2881.
- [21] B. Ferlez, M. Sutter, C. A. Kerfeld, *Metab. Eng.* **2019**, *54*, 286.
- [22] M. J. Lee, J. Mantell, I. R. Brown, J. M. Fletcher, P. Verkade, R. W. Pickersgill, D. N. Woolfson, S. Frank, M. J. Warren, *Nat. Commun.* **2018**, *9*, 3413.
- [23] H. Kirst, B. H. Ferlez, S. N. Lindner, C. A. R. Cotton, A. Bar-Even, C. A. Kerfeld, *Proc. Natl. Acad. Sci. U. S. A.* **2022**, *119*, e2116871119.
- [24] C. A. Kerfeld, M. Sutter, *Curr. Opin. Biotechnol.* **2020**, *65*, 225.
- [25] M. Sutter, M. R. Melnicki, F. Schulz, T. Woyke, C. A. Kerfeld, *Nat. Commun.* **2021**, *12*, 3809.
- [26] B. Ferlez, M. Sutter, C. A. Kerfeld, *mBio* **2019**, *10*, e02327.
- [27] T. S. Lee, R. A. Krupa, F. Zhang, M. Hajimorad, W. J. Holtz, N. Prasad, S. K. Lee, J. D. Keasling, *J. Biol. Eng.* **2011**, *5*, 12.
- [28] A. Levin-Karp, U. Barenholz, T. Bareia, M. Dayagi, L. Zelcbuch, N. Antonovsky, E. Noor, R. Milo, *ACS Synth. Biol.* **2013**, *2*, 327.
- [29] M. R. Melnicki, M. Sutter, C. A. Kerfeld, *Curr. Opin. Microbiol.* **2021**, *63*, 1.
- [30] S. D. Axen, O. Erbilgin, C. A. Kerfeld, *PLoS Comput. Biol.* **2014**, *10*, e1003898.
- [31] F. Cai, B. B. Menon, G. C. Cannon, K. J. Curry, J. M. Shively, S. Heinhorst, *PLoS One* **2009**, *4*, e7521.
- [32] M. Wheatley, S. D. Gidaniyan, Y. Liu, D. Cascio, T. O. Yeates, *Protein Sci.* **2013**, *22*, 660.
- [33] N. W. Kennedy, J. M. Hershewe, T. M. Nichols, E. W. Roth, C. D. Wilke, C. E. Mills, M. C. Jewett, D. Tullman-Ercek, *PLoS One* **2020**, *15*, e0226395.
- [34] S. Sinha, S. Cheng, C. Fan, T. A. Bobik, *J. Bacteriol.* **2012**, *194*, 1912.
- [35] P. Romero, Z. Obradovic, C. Kissinger, J. E. Villafranca, A. K. Dunker, in *Proc. Int. Conf. on Neural Networks (ICNN'97)*, vol. 1, IEEE, Piscataway, NJ, USA **1997**, pp. 90–95.
- [36] M. S. Dresselhaus, G. Dresselhaus, R. Saito, *Carbon* **1995**, *33*, 883.
- [37] S. L. Lair, W. C. Herndon, L. E. Murr, S. A. Quinones, *Carbon* **2006**, *44*, 447.
- [38] A. Luque, R. Zandi, D. Reguera, *Proc. Natl. Acad. Sci. USA* **2010**, *107*, 5323.
- [39] R. Hull, M. W. Rees, M. N. Short, *Virology* **1969**, *37*, 404.
- [40] M. Melle-Franco, G. Brinkmann, F. Zerbetto, *J. Phys. Chem. A* **2015**, *119*, 12839.
- [41] F. Mohajerani, E. Sayer, C. Neil, K. Inlow, M. F. Hagan, *ACS Nano* **2021**, *15*, 4197.
- [42] B. K. Ganser, S. Li, V. Y. Klishko, J. T. Finch, W. I. Sundquist, *Science* **1999**, *283*, 80.
- [43] G. Zhao, J. R. Perilla, E. L. Yufenyuy, X. Meng, B. Chen, J. Ning, J. Ahn, A. M. Gronenborn, K. Schulten, C. Aiken, P. Zhang, *Nature* **2013**, *497*, 643.
- [44] S. Li, C. P. Hill, W. I. Sundquist, J. T. Finch, *Nature* **2000**, *407*, 409.
- [45] H. R. Gelderblom, E. H. S. Hausmann, M. Özel, G. Pauli, M. A. Koch, *Virology* **1987**, *156*, 171.
- [46] I.-J. L. Byeon, G. Hou, Y. Han, C. L. Suiter, J. Ahn, J. Jung, C.-H. Byeon, A. M. Gronenborn, T. Polenova, *J. Am. Chem. Soc.* **2012**, *134*, 6455.
- [47] C. M. Quinn, M. Wang, M. P. Fritz, B. Runge, J. Ahn, C. Xu, J. R. Perilla, A. M. Gronenborn, T. Polenova, *Proc. Natl. Acad. Sci. USA* **2018**, *115*, 11519.
- [48] Y. Li, N. W. Kennedy, S. Li, C. E. Mills, D. Tullman-Ercek, M. O. De La Cruz, *ACS Cent. Sci.* **2021**, *7*, 658.
- [49] G. Vernizzi, R. Sknepnek, M. O. De La Cruz, *Proc. Natl. Acad. Sci. USA* **2011**, *108*, 4292.
- [50] F. Mohajerani, M. F. Hagan, *PLoS Comput Biol.* **2018**, *14*, e1006351.
- [51] D. G. Gibson, L. Young, R.-Y. Chuang, J. C. Venter, C. A. Hutchison, H. O. Smith, *Nat. Methods* **2009**, *6*, 343.
- [52] A. Shevchenko, M. Wilm, O. Vorm, M. Mann, *Anal. Chem.* **1996**, *68*, 850.
- [53] W. F. Tivol, A. Briegel, G. J. Jensen, *Microsc. Microanal.* **2008**, *14*, 375.
- [54] M. Schorb, I. Haberbosch, W. J. H. Hagen, Y. Schwab, D. N. Mastrodonato, *Nat. Methods* **2019**, *16*, 471.
- [55] J. Zivanov, T. Nakane, B. O. Forsberg, D. Kimanius, W. J. Hagen, E. Lindahl, S. H. Scheres, *Elife* **2018**, *7*, e42166.
- [56] J. Zivanov, T. Nakane, S. H. W. Scheres, *IUCrj* **2020**, *7*, 253.
- [57] A. Rohou, N. Grigorieff, *J. Struct. Biol.* **2015**, *192*, 216.
- [58] M. D. Hanwell, D. E. Curtis, D. C. Lonie, T. Vandermeersch, E. Zurek, G. R. Hutchison, *J. Cheminf.* **2012**, *4*, 17.